Resonance modes of a metal-semiconductor-metal multilayer mediated by electric charge

Journal of Physics Communications

OPEN ACCESS

RECEIVED
23 March 2022

REVISED
9 April 2022

ACCEPTED FOR PUBLICATION
14 April 2022

PUBLISHED
25 April 2022

PAPER

Resonance modes of a metal-semiconductor-metal multilayer mediated by electric charge

Kazuma Isobe[1,2] **and Katsunori Hanamura**[1]

[1] School of Engineering, Department of Mechanical Engineering, Tokyo Institute of Technology, Ookayama 2-21-1, Meguro-ku, Tokyo 152-8550, Japan

[2] Department of Advanced Mechanics, Graduate School of Natural Science and Technology, Okayama University, Tsushima-naka 3-1-1, Kita-ku, Okayama 700-8530, Japan

E-mail: isobe.k.ad@okayama-u.ac.jp

Keywords: resonance modes, finite difference time domain method, metal–semiconductor–metal multilayer, lumped-element model, Fabry–Pérot interference, surface plasmon polariton, electric charge

Abstract

Electromagnetic fields around metal–semiconductor–metal (MSM) multilayers with square island top layers were numerically simulated to elucidate the difference in physics between the circuit resonance and Fabry–Pérot interference mediated by the surface plasmon polaritons (SPP). In the current study, the top and bottom metal layers were made of gold, and the intermediate semiconductor layer was a gallium antimony (GaSb). The lumped-element and Fabry–Pérot interference models showed less accuracy when the island width of the MSM multilayer was comparatively smaller. Since the capacitor and SPP could not be supported between the top and bottom gold layers, the anti-reflection mode of the gold–GaSb bilayer mainly affected the absorptance. However, when the width of the island was sufficiently large, the time-lapse development of the electromagnetic fields at resonant wavelengths showed strong electric and magnetic responses relating to the circuit resonance. Simultaneously, the electric fields depicted the movement of the electric charge, which coupled to the short-range surface plasmon polariton (SRSP) existing at the thin GaSb layer sandwiched by two gold layers. The wavelength of the SRSP approximately corresponded to that of the Fabry–Pérot interference. It was revealed that the lumped-element and Fabry–Pérot interference models indicated the same resonant mode from two different perspectives in physics.

1. Introduction

Electromagnetic metamaterials have attracted the attention of many scientists investigating applications of negative refraction [1], optical cloaking [2], perfect blackbodies [3], and wavelength-selective emitters and absorbers [4–8], among others. These metamaterials consist of various nano/micro-structures that manipulate the propagation behavior of electromagnetic waves at wavelengths longer than their structures. As candidate metamaterials, a one-dimensional grating [5, 9], split-ring resonators [10], three-dimensional porous materials [11], and an aperiodic multilayer [12] were proposed over the past several years. To reveal the physics establishing the metamaterials, the electromagnetic properties of these metamaterials were often evaluated using numerical analysis methods, such as finite difference time domain (FDTD) or rigorous coupled wave analysis (RCWA). Concurrently, the resonant frequencies of the metamaterials were formulated using equivalent physical models. A representative model is a lumped-element model that expresses a group oscillation of free electrons and electric current inside a nano/micro-structure as an electric circuit [13–15]. An electromagnetic wave at the resonant frequency is almost perfectly absorbed because the electric impedance of the circuit is zero at such a frequency. Researchers in the fields of engineering and optics studied the magnetic properties of such circuits and identified metamaterials with negative magnetic permeabilities at resonant frequencies [4, 16–18]. Several researchers coined a term for the resonance at a frequency with negative permeability, a magnetic plasmon polariton (MPP) [19, 20] or simply a magnetic polariton (MP) [4, 5, 9, 21–23]. This is an analogy for the

surface plasmon polariton (SPP) at a frequency with negative permittivity. The zero-impedance frequencies of nanostructures have been theoretically and experimentally studied. For example, the electromagnetic properties of metal–insulator–metal (MIM) [21, 24], metal–dielectric–metal (MDM) [25], and metal–semiconductor–metal (MSM) [26, 27] multilayers have been studied for over 20 years. Here, the top metal layer can have a rectangular [21, 24, 28], cross [21, 29], or split-ring shape [10, 18, 30], among others. Since their significant absorptive and emissive characteristics are useful to improve the efficiency of thermophotovoltaic (TPV) power generation, MSM multilayers using a TPV semiconductor, e.g., gallium antimony (GaSb), were proposed to selectively absorb thermal radiation exceeding the bandgap energy level [26, 27]. Moreover, a MIM multilayer used as a frequency-tunable emitter is also a convenient way to provide such a radiation to a TPV cell [4].

The discussions about the lumped-element model relating to MPs have been developed; however, they sometimes evaded several fundamental questions. At first, the suffix '-on' in 'polariton' indicates a quantum or elementary particle. While an SPP originates a plasmon, the quantized group oscillation of the electric charge, past studies of MPPs and MPs have not revealed the existence of an equivalent quantum. If it corresponds to a magnon, the quantized spin wave related to the magnetism [31, 32], the resonant phenomena should be called magnon polariton [31]. However, the magnon frequency is usually a few GHz, which is ordinary difficult to exhibit a magnetic response at the near-infrared regime [31]. At second, the magnetic response at the resonant frequency is often investigated independently from an electric or a plasmonic response of the nanostructures. Several studies showed a relation between the resonant mode and classical Fabry–Pérot interference, which is an electrical response originated by a propagating wave or SPP [26, 27, 33]. Wang and Zhang declared that the MP and Fabry–Pérot interference have individual physics and are distinguishable [23]. However, few perspectives for both the magnetic response at the Fabry–Pérot interference frequency and the behavior of SPP at the MP frequency might result in misunderstandings of the nature of resonance. Because the electric and magnetic responses are not independent considering Maxwell's equations, the SPP affects both the electric and magnetic fields around the nanostructures. In the current study, time-step developments of the electromagnetic fields around MSM multilayers of various dimensions are numerically analyzed to simultaneously display the magnetic field and the electric charge, the origin of SPP. Moreover, each resonant mode is theoretically compared with the lumped-element and Fabry–Pérot interference models. The distinguishability of the MP and Fabry–Pérot interference are discussed through numerical and theoretical approaches.

2. Numerical simulation

In the current study, Maxwell's equations for electromagnetic fields were numerically solved using a three dimensional FDTD approach. This was done to obtain the spectral absorptance of the MSM multilayer and to show the electromagnetic field around them [34]. The simulation was conducted using a Fortran program developed by the authors. The simulation results for the representative case were validated using data obtained employing other open-source software such as MEEP [35]. Figure 1 shows a schematic representation of the MSM multilayer. The bottom and top metal layers are made of gold, while the semiconductor, a GaSb layer, is sandwiched between the gold layers. The relative magnetic permeabilities of GaSb and gold were set to be 1.0. The complex permittivity of gold [36] was fitted according to the monopole Drude model:

$$\varepsilon(\omega) = \varepsilon' + i\varepsilon'' = \varepsilon_\infty - \frac{\omega_{\mathrm{Drude}}^2}{\omega(\omega + i\Gamma_{\mathrm{Drude}})}, \tag{1}$$

while that of GaSb [37] was fitted using the monopole Lorentz model:

$$\varepsilon(\omega) = \varepsilon' + i\varepsilon'' = \varepsilon_\infty + \frac{f_{\mathrm{Lorentz}}\omega_{\mathrm{Lorentz}}^2}{\omega_{\mathrm{Lorentz}}^2 - \omega^2 - i\Gamma_{\mathrm{Lorentz}}\omega}. \tag{2}$$

Here, ε_∞ is the respective permittivity at an infinite angular frequency, ω_{Drude} is the plasma frequency, Γ_{Drude} is the carrier relaxation rate, f_{Lorentz} represents the strength of the Lorentz oscillator, $\omega_{\mathrm{Lorentz}}$ is the central frequency of the Lorentz oscillator, and $\Gamma_{\mathrm{Lorentz}}$ is the damping factor. Table 1 shows each of these parameters for the two materials used to construct the MSM multilayer in the current study. These optical properties were introduced into the simulation using a piecewise linear recursive convolution method [38].

The configuration of the MSM multilayer, referred to as the island geometry, is shown in figure 1. The characteristic parameters are defined as follows: w and l respectively show the x- and y- directional island widths, h (=100 nm) is the height of the top gold layer, Λ is the pitch length of each unit cell, and d (=100 nm) is the thickness of the semiconductor. A square configuration was assumed with $w = l$ in this study to focus on the simplified resonant mode excited around an isotropic geometry. Since this study aims to analyze electromagnetic fields, especially at a thin semiconductor layer, the island height, h, was fixed at a constant value to simplify the discussion. The thickness of the gold bottom layer, 200 nm, is sufficient to eliminate transmission

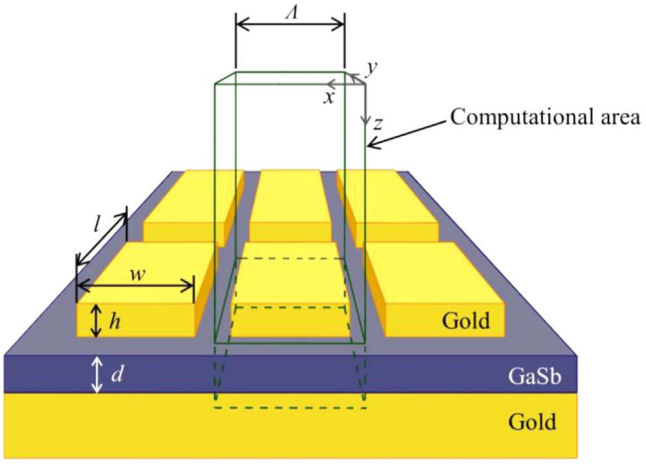

Figure 1. Schematic diagrams of the MSM multilayer consisting of a top square-island arrangement and a smooth bottom substrate made of gold. The thin intermediate layer consists of gallium antimony (GaSb).

Table 1. Fitting parameters of dielectric functions.

Parameters	Gold	GaSb
ε_∞ (—)	3.9703	8.2721
ω_{Drude} (rad/s)	1.2118×10^{16}	—
Γ_{Drude} (rad/s)	1.2346×10^{14}	—
f_{Lorentz} (—)	—	5.8918
$\omega_{\mathrm{Lorentz}}$ (rad/s)	—	3.7035×10^{15}
$\Gamma_{\mathrm{Lorentz}}$ (rad/s)	—	1.5012×10^{15}

of near-infrared rays. So, the spectral absorptance of the multilayer can be calculated from the intensity ratio of the difference between the incident and reflected rays to the incident ray. One period of each multilayer is set in the computational area, as depicted by the green lines in figure 1. The side boundaries of computational area are a simple periodic boundary condition, while both the top and bottom boundaries are set as a second-order perfectly matched layer (PML) [39, 40]. The spectral absorptance of the MSM multilayer was evaluated using an E_x-polarized plane wave that was generated at the top boundary for the incident rays and vertically irradiated the multilayer. The spatial resolution of computational grid was 5.0 nm and the time resolution was 5.0×10^{-18} s.

In this study, simulations were conducted using the TSUBAME 3.0 supercomputer of the Global Scientific Information and Computing Center at the Tokyo Institute of Technology and a personal workstation with a multi-core processor (Ryzen Threadripper 3970X; AMD, Santa Clara, California, United States).

3. Theoretical models

3.1. Lumped-element model

Figure 2(a) shows a schematic of the representative lumped-element or circuit model proposed by several researchers over the past 20 years [4, 28, 41]. Here, the electric current in the metal layer originates from a group oscillation of free electrons oscillated by an incident ray. When its oscillation frequency is higher than the reciprocal of the Drude relaxation time of the metal, the group oscillation of the free electrons contributes to forming a capacitor and inductor that modulate the multilayer absorptance. For gold, the relaxation time is 3.0×10^{-14} s and its reciprocal is 3.3×10^{13} Hz [42]. Thus, radiation with wavelengths shorter than 9.0 μm contributes to the group oscillation. In this study, mutual inductance between the top and bottom gold layers and kinetic inductance inside the gold slab, L_{m} and L_{k}, are defined as follows:

$$L_{\mathrm{m}} = 0.5\mu_0 \frac{wd}{l}. \tag{3}$$

$$L_{\mathrm{k}} = -\frac{w}{\varepsilon_0 \omega^2 l \delta} \frac{\varepsilon'_{\mathrm{Au}}}{\varepsilon'^2_{\mathrm{Au}} + \varepsilon''^2_{\mathrm{Au}}}. \tag{4}$$

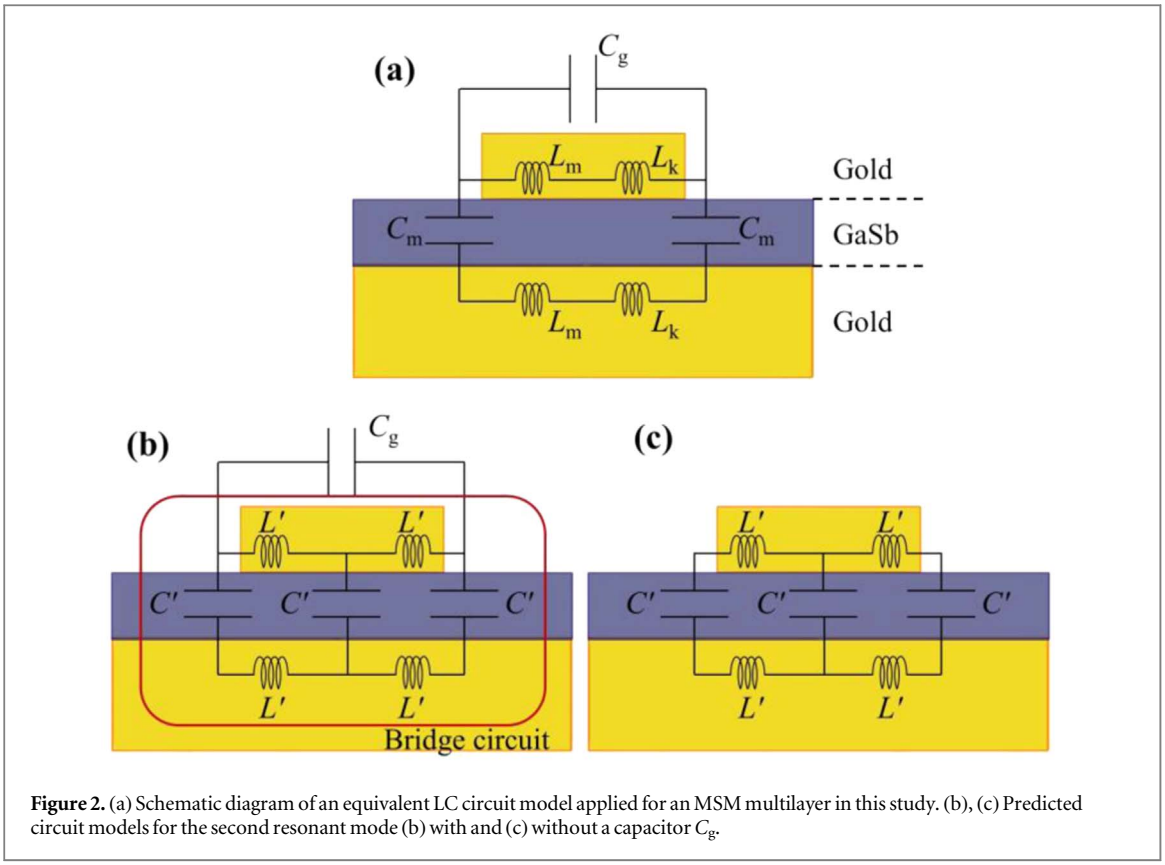

Figure 2. (a) Schematic diagram of an equivalent LC circuit model applied for an MSM multilayer in this study. (b), (c) Predicted circuit models for the second resonant mode (b) with and (c) without a capacitor C_g.

where $\delta = c_0/2\omega\kappa_{Au}$ is the penetration depth of the electromagnetic wave inside gold, which is the length that the intensity of incident wave attenuates at a rate of e^{-1}, and $\kappa_{Au} = \sqrt{(-\varepsilon'_{Au} + \sqrt{\varepsilon'^2_{Au} + \varepsilon''^2_{Au}})/2}$ is the extinction coefficient of gold. Additionally, the capacitance values between the top and bottom metal layers, C_m, and between the two islands, C_g, are defined as follows:

$$C_m(\omega) = c'\varepsilon'_{GaSb}\,\varepsilon_0\frac{wl}{d}, \tag{5}$$

$$C_g(\omega) = \varepsilon_0 A\frac{hl}{\Lambda - w}, \tag{6}$$

where, ε'_{GaSb} is the real permittivity of GaSb. The imaginary part, $\varepsilon'G_{aSb}$, does not affect the capacitance. The parameter, c', is a factor to account for the fringe effects of an electric field around the island layer. Generally, c', has a value in the range of 0.2 to 0.3 [21, 23, 27, 41, 43]. The non-dimensional constant, $A = 8.0$, is an empirical parameter introduced in this study to amplify C_g under conditions with narrow channels. Finally, the total impedance of the circuit shown in figure 2(a) is described as:

$$Z_{total}(\omega) = i\omega\left(\frac{L_m + L_k}{1 - \omega^2 C_g(L_m + L_k)} - \frac{2}{\omega^2 C_m} + L_m + L_k\right) \tag{7}$$

When $Z_{total}(\omega_r)$ becomes zero, the free electrons inside an island oscillate without resistance. The resonant angular frequency, ω_r, can be mathematically calculated as follows:

$$\omega_r = \sqrt{\frac{C_g + C_m \pm \sqrt{C_g^2 + C_m^2}}{C_g C_m(L_m + L_k)}} \tag{8}$$

ω_r with a positive value of $\sqrt{C_g^2 + C_m^2}$ corresponds to an ultraviolet ray. Thus, a negative value of $\sqrt{C_g^2 + C_m^2}$ is the only meaningful solution. It is notable that $Z_{total}(\omega_r)$ can be zero at more than two frequencies because permittivities have an angular frequency dependency. The resonance at the circuit model was correlated with the absorption of electromagnetic waves at the semiconductor layer. Oscillation of free electrons produces a current loop between the island and bottom gold layer. As a result, a strong magnetic field is excited at the semiconductor or insulator layer, as reported in an earlier study and referred to as MP [4, 5, 23]. Moreover, several resonant modes at higher-order modes, originated by an LC circuit with multiple capacitors and inductors, have been called MP2, MP3, and so on. Figure 2(b) shows a predicted circuit model for the second resonant mode corresponding to MP2. Divided capacitors, C', and inductors, L', are correlated to C_m, L_m, and L_k as follows:

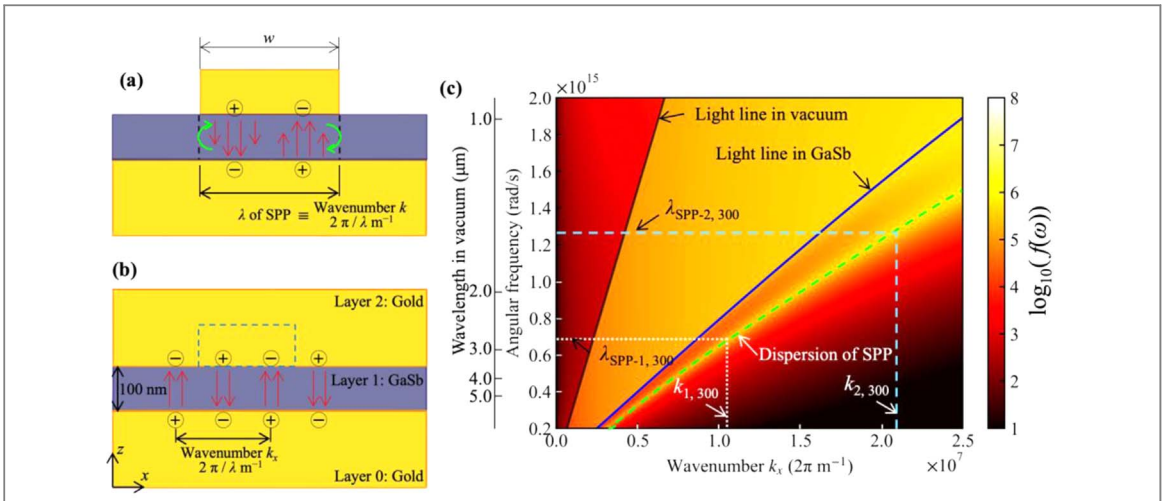

Figure 3. (a) The model of Fabry–Pérot interference parallel to the interface between vacuum and semiconductor layers. (b) Schematic diagram of the SPP inside a GaSb layer between two smooth gold planes. (c) The magnitude of dispersion relation $f(\omega)$ at a GaSb layer is depicted by contours. The local maximum of $f(\omega)$ that indicates the dispersion of the SPP is shown as a green dotted line.

$$C' = \frac{2}{3}C_{\mathrm{m}}, \tag{9}$$

$$L' = \frac{1}{2}(L_{\mathrm{m}} + L_{\mathrm{k}}) \tag{10}$$

In figure 2(b), the red circled area works as a bridge circuit. Since the capacitors and inductors stand symmetrically, the capacitor C' at the center of the island can be neglected. Therefore, the total impedance of the circuit is described as follows:

$$Z_{\mathrm{total}}(\omega) = i\omega\left(\frac{2L'}{1 - 2\omega^2 C_{\mathrm{g}} L'} - \frac{2}{\omega^2 C'} + 2L'\right) \tag{11}$$

Figure 2(c) shows another predicted model that ignores the contribution of the capacitor, C_{g}. The total impedance of the circuit and resonant angular frequency can be written as follows:

$$Z_{\mathrm{total}}(\omega) = i\omega\left(2L' - \frac{1}{\omega^2 C'}\right)\left(1 + \frac{1}{2 - 2\omega^2 L' C'}\right), \tag{12}$$

$$\omega_{\mathrm{r}} = \sqrt{\frac{3}{2C_{\mathrm{m}}(L_{\mathrm{m}} + L_{\mathrm{k}})}}, \frac{3}{\sqrt{2C_{\mathrm{m}}(L_{\mathrm{m}} + L_{\mathrm{k}})}} \tag{13}$$

Here, $\omega_{\mathrm{r}} = \sqrt{3/2C_{\mathrm{m}}(L_{\mathrm{m}} + L_{\mathrm{k}})}$, corresponds to the eigenmode frequency for a limited part of the circuit. Thus, only $\omega_{\mathrm{r}} = 3/\sqrt{2C_{\mathrm{m}}(L_{\mathrm{m}} + L_{\mathrm{k}})}$ is the frequency related to the absorption of an electromagnetic wave.

3.2. Interference of surface plasmon polaritons

Fabry–Pérot interferences are possible physics relating to the electric response for an MSM multilayer. Ni *et al* described a Fabry–Pérot interference in a perpendicular direction to the vacuum–semiconductor interface that exhibited a resonant peak independent of an island or grating width, w [27]. In this case, an electromagnetic wave exhibited a Fabry–Pérot interference as a propagating mode. However, Liu and Takahara proposed another Fabry–Pérot interference model in a parallel direction to the interface and described that its resonant peak exhibits an island width dependency [33]. The resonant mode satisfies following relation:

$$kw + \phi = m\pi, \tag{14}$$

where, k, ϕ, and m respectively denote the wavenumber of the resonant mode, phase retardation, and the order of the resonant mode ($m = 1, 2, 3\ldots$). Figure 3(a) shows a schematic of the interference inside the semiconductor layer. Since the semiconductor thickness, d, is much shorter than the wavelength of the incident infrared ray, the incident wave cannot penetrate into the area sandwiched by the top and bottom metal layers as a propagating mode. Instead, the incident wave produces a polarization of the electric charges at the lower surface of the island and the upper surface of the bottom layer. Therefore, the incident wave couples with a transverse magnetic (TM) mode of an SPP supported by the longitudinal oscillation of electric charge and is permitted to enter the semiconductor layer. It is notable that the wavelength of the SPP is not the same as that of the propagation mode at vacuum. A rigorous relation between the angular frequency of the incident ray and the

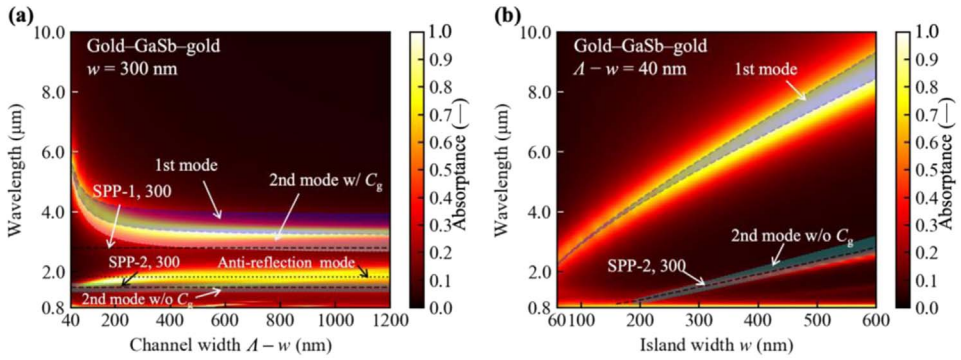

Figure 4. Spectral absorptances of an MSM multilayer under various conditions are depicted in a contour plot. (a) The channel width between the two islands $\Lambda - w$ is fixed at 40 nm. (b) The island width, w, is fixed at 300 nm. Resonant wavelengths indicated by the lumped-element model for the first mode, the second mode with and without C_g are respectively depicted as blue, white, and light blue bands. The wavelengths indicated by the interference of the SPP are expressed by dotted black lines.

wavenumber of the SPP, i.e., dispersion relation, is difficult to derive for the MSM multilayer shown in figure 3(a).

As an approximation, a dispersion relation at the GaSb layer sandwiched by two parallel infinite gold planes, shown in figure 3(b), can be numerically determined. The dispersion relation of the SPP is separately expressed for propagating and evanescent components as [44]:

$$f^{\mathrm{prop}}_{\mathrm{TM},02}(\omega) = \frac{1}{4\pi^2}\int_0^{\omega/c_0} \frac{(1-|r_{10}^{\mathrm{TM}}|^2)(1-|r_{12}^{\mathrm{TM}}|^2)}{|1-r_{10}^{\mathrm{TM}}r_{12}^{\mathrm{TM}}e^{2ik'_{z1}d}|^2}k_x\,\mathrm{d}k_x, \tag{15}$$

$$f^{\mathrm{evan}}_{\mathrm{TM},02}(\omega) = \frac{1}{\pi^2}\int_{\omega/c_0}^{\infty} \frac{\mathrm{Im}(r_{10}^{\mathrm{TM}})\mathrm{Im}(r_{12}^{\mathrm{TM}})}{|1-r_{10}^{\mathrm{TM}}r_{12}^{\mathrm{TM}}e^{-2k''_{z1}d}|^2}e^{-2k''_{z1}d}k_x\,\mathrm{d}k_x, \tag{16}$$

where k_x and k_{z1} are wavenumbers of the SP in the x- and z-directions, r_{ij} is the reflection coefficient between media i and j. The green dotted line in figure 3(c) corresponds to dispersion relations of the SPP oscillated inside the GaSb layer [45]. In this figure, the black and blue solid lines indicate light lines in a vacuum and in GaSb, respectively, depending on their refractive indices. The dispersion relation of the SPP exists at a higher wavenumber than the light line in the GaSb layer. Then, the wavelength of the SPP is smaller than that of a propagating wave in the GaSb layer. The wavenumber involving the Fabry–Pérot interference can be derived using the dispersion relation. According to equation (14), the wavenumber of the interfered wave becomes $(m\pi - \phi)/w$ with a unit of $2\pi/\mathrm{m}$. Dotted white and light blue vertical lines in figure 3(c) respectively show the wavenumbers, $k_{1,300}$ and $k_{2,300}$, corresponding to the first and second interference modes with $w = 300$ nm, assuming the phase retardation, ϕ, is zero. Then, the Fabry–Pérot interference model estimates the first and second peak wavelengths, $\lambda_{\mathrm{SPP}-1,300} = 2.8\,\mu\mathrm{m}$ and $\lambda_{\mathrm{SPP}-2,300} = 1.49\,\mu\mathrm{m}$. Note that the phase retardation is usually larger than zero; thus, the peak slightly redshifts from the prediction [33].

4. Simulation results and discussion

4.1. Simulation results

Figure 4(a) shows a contour plot of the spectral absorptance for an MSM multilayer with various channel widths between islands, $\Lambda - w$, while the island width was fixed at 300 nm. Two absorptance peaks asymptotically approach the wavelengths of 3.3 and 1.84 μm, respectively, with increased channel width, $\Lambda - w$. The blue band, calculated using the circuit model in equation (7) employing a fringe factor, c', from 0.2 to 0.3, well superposes on the peak at 3.3 μm. The lumped-element model describes the beginning of the peak for any channel width. Using no amplification constant, A, the circuit model indicated a shorter wavelength range, from 3.42 to 4.07 μm, for a channel width of 40 nm. Although the constant, A, was not rigorously based on physics, it improved the accuracy of the lumped-element model for channels narrower than the island width. However, the first interference wavelength of the SPP (SPP-1, 300) slightly deviates from the peak wavelength compared to the lumped-element model. It is because the phase retardation of the Fabry–Pérot interference was assumed to be zero in the current calculation. In order to reduce the discrepancy, the phase retardation should be 0.17π, which is consistent with the past study [33]. Contrary to the first peak, the lumped-element model shows diminished accuracy for the second mode at 1.84 μm. The white and light blue bands respectively depict the range of the second resonant wavelengths calculated using equations (11) and (12). The estimated model including C_g

exhibits a wavelength close to the first rather than the second mode. Another model with no C_g indicates a range from 1.33 to 1.62 μm, which is much closer to the peak. These results imply that equation (12) is adequate to express the impedance related to the second mode of circuit resonance, and the second mode is independent of C_g. Here, the second interference wavelength of the SPP (SPP-2, 300) is the same as the peak wavelength with a channel width, $\Lambda - w$, of 40 nm. The second peak slightly redshifts with increasing channel width and approaches 1.84 μm, which corresponds to the anti-reflection mode or the Fabry–Pérot interference of the gold–GaSb bilayer for the propagation wave. The spectral absorptance of the bilayer is simply calculated using the following formula [34]:

$$\alpha(\lambda) = 1 - \left| \frac{r_{01} + r_{12}\exp(i2\beta)}{1 + r_{01}r_{12}\exp(i2\beta)} \right|^2 \tag{17}$$

where, $\beta = 2\pi d N_1 \cos\theta_1/\lambda$ is the phase shift in the GaSb layer, N_1 ($=n_1 + i\kappa_1 = \sqrt{\varepsilon_{\mathrm{GaSb}}}$) is the complex refractive index of GaSb, while θ_1 is a refraction angle. For the normal incidence with $\theta_1 = 0$, the approximate wavelength of the first peak is $4n_1 d$ while κ_1 affects a slight peak shift.

Figure 4(b) shows a contour plot of spectral absorptance for an MSM multilayer with various island widths, $w = l$, and a fixed channel width between two islands, $\Lambda - w = 40$ nm. A series of wide band peaks, which redshift proportional to the island width, $w = l$, is observed in the region from 2.5 to 9.0 μm for the range of island widths from 60 to 600 nm. The lumped-element model for the first mode also exhibits a redshift trend and similar values. Moreover, the wavelengths indicated by the two models, i.e., the lumped-element model for the second mode with no C_g and the interference model, superpose on the secondary peak in the range of 1.0 to 2.5 μm. Although these two models have different backgrounds in physics, the lumped-element model may essentially indicate the resonant wavelength at which the SPP oscillates interfered by the island width.

4.2. Second resonant mode

Figure 5(a) shows the electromagnetic field distributions around the MSM multilayer at the second peak wavelength, 1.49 μm. The island and channel widths, w and $\Lambda - w$, were respectively 300 and 40 nm. At $t = 0$, the lower left and right corners of the island were respectively charged positively and negatively. As a counterpart, opposite electric charges were observed at the surface of the bottom gold layer. As progressing time, these electric charges gradually shifted to the center and formed a longitudinal wave at the lower surface of the island and the upper surface of the bottom layer. These longitudinal waves are the odd mode of the SPP, called the short-range surface plasmon polariton (SRSP) [46]. The SPP exhibits a strong electric field in the z-direction, E_z, observed at the quarter length of the island width from the lower corners of the island at $t = T/4$ s, where T is one wave period. The electric charges shifted to the center until $t = 5T/12$ s. However, the charges from the left and right sides canceled each other in the next $T/12$ s. At $t = T/2$ s, the lower left and right corners of the island have opposite charges to those at $t = 0$ s. These electric charges alternately switch at an interval of a half period, $T/2$ s. E_z below the lower island corners and center, as shown by the dotted red lines in figure 5(a), were kept at almost zero through one cycle. This is because the longitudinal wave and SPP generated at the lower left and right island corners have opposite phases and interfered with each other. Here, the distances between each node are almost half an island width. Thus, the wavenumber of the SPP satisfies the relation in equation (14) with $m = 2$. Moreover, the y-directional magnetic field, H_y, exhibits high intensities at the center and lower corners of the island at $t = 0$ s. The intensity of H_y drastically diminishes at $t = T/4$ s and recovers at $t = T/2$ s. Through one cycle, H_y is kept at zero at the quarter length of the island from the bottom corners of the island, as depicted by dotted green lines in figure 5(a). H_y shows a maximum amplitude $T/4$ s earlier than E_z, and there are differences in the node position by a quarter wavelength. These gaps in time and space for the electromagnetic field are a classical feature of stationary waves observed at the interferometer.

Figure 5(b) shows the distribution of the electric field for $\Lambda = 900$ nm and $w = 300$ nm at the second peak wavelength, 1.84 μm. When the phase retardation in equation (14) is zero, the left and right nodes for E_z should be fixed at the two geometric edges described by the dotted yellow lines in this figure. However, the electric field did not clearly exhibit two nodes due to expansion of the electric field in the GaSb layer to a region outside the geometric edge lines. Similarly, the node for H_y shifted closer to the geometric edge, and it shows an expansion of the SPP wavelength. This is because electric charges at the lower surface are less affected by those of nearby islands compared to the case where $\Lambda = 340$ nm. Therefore, the wavelength of the longitudinal wave increased by approximately 80 nm with expanding distance between the positive and negative charges, and it causes a phase retardation. The phase retardation caused a redshift of the second resonant peak, and the peak superposes on the anti-reflection mode of the gold–GaSb bilayer. With smaller island widths compared to the pitch, Λ, the SPP mode less affected the resonant wavelength while a part of the propagation wave coupled with the SPP.

The abovementioned electromagnetic field also can be described using the lumped-element model for the second resonant mode. Figure 5(c) shows a schematic diagram of the electric charge adapted to the lumped-

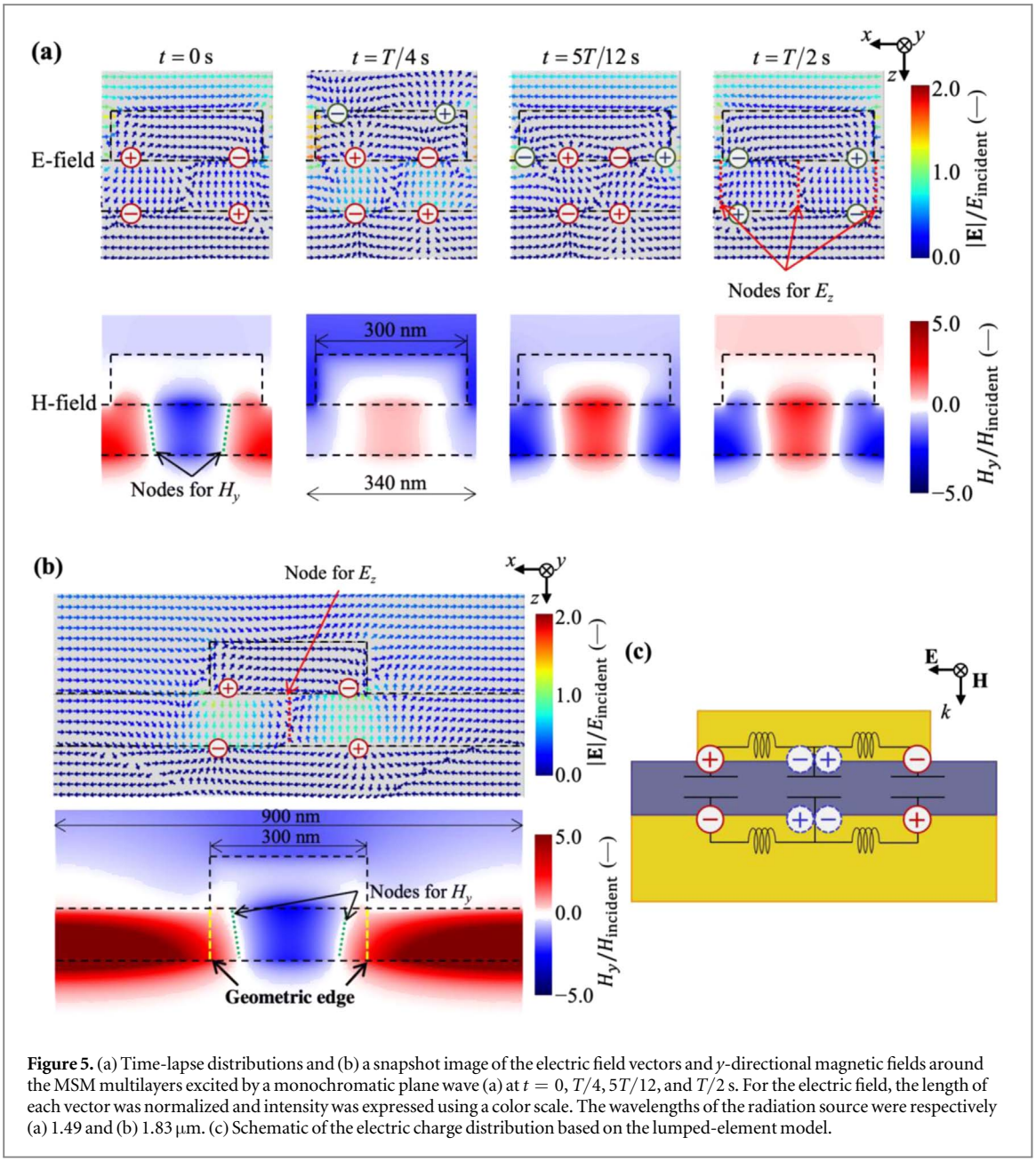

Figure 5. (a) Time-lapse distributions and (b) a snapshot image of the electric field vectors and y-directional magnetic fields around the MSM multilayers excited by a monochromatic plane wave (a) at $t = 0$, $T/4$, $5T/12$, and $T/2$ s. For the electric field, the length of each vector was normalized and intensity was expressed using a color scale. The wavelengths of the radiation source were respectively (a) 1.49 and (b) 1.83 μm. (c) Schematic of the electric charge distribution based on the lumped-element model.

element model. The electric charges are localized anti-symmetrically inside the island layer when the incident wave vertically irradiates the MSM multilayer. These electric charges form two capacitors with opposite charges at the left and right sides of the circuit. Here, two adjacent capacitors should be oppositely charged at the resonant mode. Consequently, the electric charge at the central capacitor is canceled and kept at zero. Despite no electric charge, the capacitor still affects the resonant frequency. Thus, the lumped-element model for the second mode, corresponds to the MP2 mode in previous studies, approximately exhibits the peak wavelength. However, the electromagnetic field distribution in figure 5 is different from the MP2 mode and similar to the MP3 mode because a previous study observed symmetrical electric charges inside the island layer using an inclined incident wave [4]. These results reveal that simulations with different incident angles cause different distributions in the magnetic fields for each resonant mode. Regardless of the incident angle and magnetic field, the wavelength of the SPP and the lumped-element model can clearly show that the second peak is the second resonant mode.

4.3. First resonant mode

Figure 6(a) depicts a time-lapse development of the electromagnetic field around the MSM multilayer at the wavelength of the first peak, 5.45 μm for $\Lambda - w = 40$ nm and $w = l = 300$ nm. At $t = 0$ s, H_y in the negative direction of the y-axis was strongly confined inside the GaSb layer, and the electric flux lines showed a circular current loop in the anticlockwise direction. The current loop disappeared at $t = T/36$ s, and the electric charge

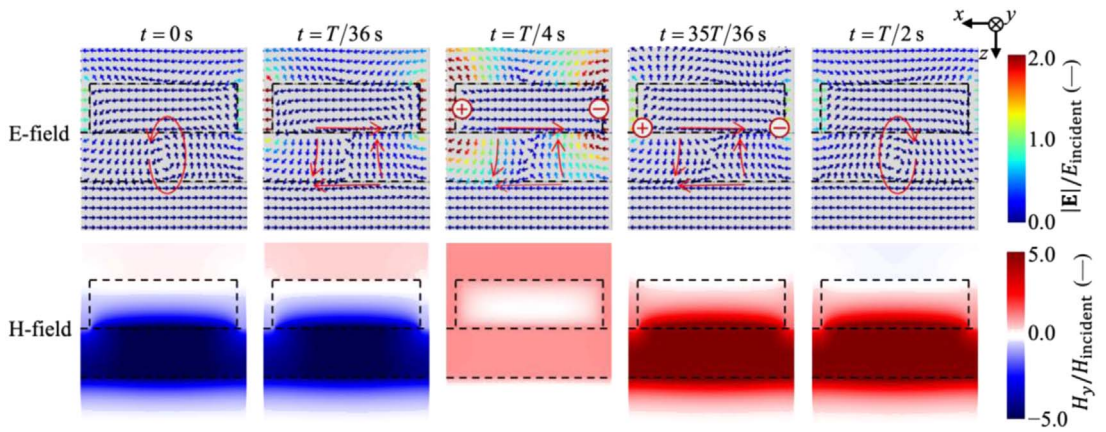

Figure 6. Time-lapse distributions of the electric field vectors and y-directional magnetic fields around the MSM multilayers excited by a monochromatic plane wave at $t = 0$, $T/36$, $T/4$, $35T/36$, and $T/2$ s. The wavelength of the radiation source was 5.45 μm. The length of each vector was normalized and intensity is expressed using a color scale.

started to localize at the left and right sides of the island over $8T/36$ s. At $t = T/4$ s, the localized charges formed a strong electric field at the vacuum gap between two islands. The electric field expanded into the vacuum region above the island. Simultaneously, the electric field was attenuated along the interface between GaSb and gold. These results show that the effective wavelength of the SPP extended to $w + 2h$, keeping the phase retardation at 0.17π. This irregular expansion of the SPP caused the discrepancy from the first peak. The expansion also affected the lumped-element model. The electric field corresponding to the capacitor C_g was stronger than C_m, although C_m is numerically larger than C_g. The constant, A, in equation (6) reduces deviation between the lumped-element model and the exact electromagnetic field around the multilayer with a narrow channel, and improves the accuracy of the lumped-element model.

At $t = T/4$ s, H_y at the GaSb layer exhibited the same magnitude as the incident wave since there is a gap in time when the electric and magnetic fields each reach maximum amplitudes. The magnetic field was confined and amplified in the positive direction of the y-axis over the next $T/4$ s as the localized electric charge dissipated. A current loop in the clockwise direction was observed at $t = T/2$ s. The current loop was formed at a time after $t = 35T/36$ s, when the magnetic field had finished recovering. Although previous research indicated that the electrical loop significantly induced a magnetic field and MP [4, 21, 23], the loop was observed during only a little moment in the time-lapse development of the electric field. The current loop seems to be a temporary state existing during the switching of the electric charge. Since the SRSP mode controls the oscillation of the electric charge, the SPP should be the origin of both the electric and magnetic responses observed around the MSM multilayer. These results supports that the Fabry–Pérot interference model for the SRSP mode indicated the same resonant mode as the lumped-element model, which shows the resonant frequency of the MP.

4.4. Critical point for the circuit resonance

Figure 7 shows a contour plot of spectral absorptance with a fixed island width, $w = 100$ nm. The resonant wavelength of the lumped-element model deviates from the absorptance peak when the channel width is larger than 100 nm. Moreover, the peak wavelength almost perfectly superposes the anti-reflection mode of the gold–GaSb bilayer. Thus, the island layer and circuit resonance less affect the resonant wavelength with increasing channel width. Furthermore, the spectral absorptance of the MSM multilayer asymptotically approaches that of the gold–GaSb bilayer. Both the Fabry–Pérot interference and lumped-element models lose accuracy when the island width is comparable to the semiconductor thickness.

Figure 8(a) depicts the electric field vector around an MSM multilayer with a structure of $\Lambda - w = 600$ nm and $w = l = 300$ nm, which is a geometry where the lumped-element model accurately exhibits the peak wavelength. The electric field was oscillated by an incident ray with a wavelength of 3.33 μm corresponding to the absorptance peak. The E_z, have opposite directions at the upper and lower surfaces of the island layer. It can be clearly seen that the lower left and the right corners of the rectangular island are, respectively, positively and negatively charged. The substrate directly below the island is charged negatively and positively as counterparts of the electric charges in the island. These electric charges are the SRSP inside the gold layer, and promote two capacitors, C_m, at the left and right halves of the island layer.

Figure 8(b) shows the electromagnetic field distribution around the MSM multilayer with a structure such that $\Lambda - w = 800$ nm and $w = l = 100$ nm. The wavelength of the incident wave corresponds to the first peak,

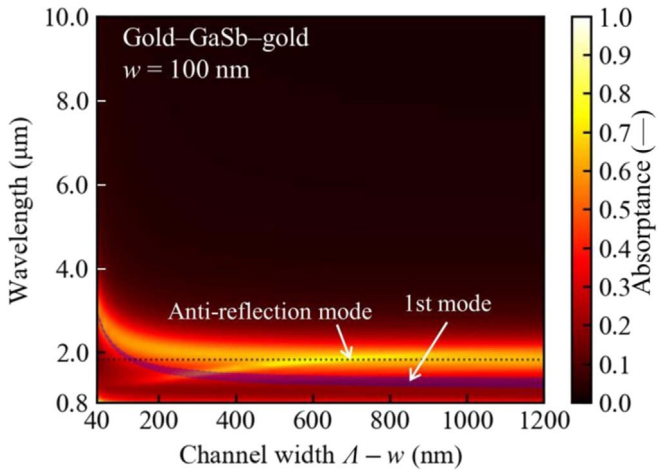

Figure 7. Spectral absorptance of MSM multilayer under various conditions of channel width between the two islands, $\Lambda - w$, is depicted in a contour plot. The island width, w, is fixed at 100 nm. Resonant wavelength indicated by the lumped-element model for the first mode is depicted by a blue band.

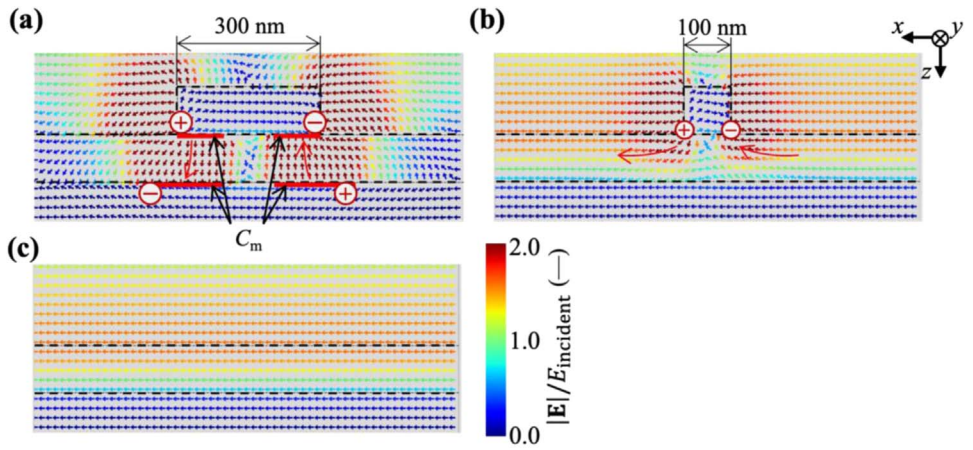

Figure 8. Imagery of the electric fields around the MSM multilayers at the moment the electric fields exhibiting maximum intensities. The pitches of the periodic structures, Λ, are fixed at 900 nm. The island widths are respectively (a) 300 nm, (b) 100 nm, and (c) no island. The electric fields were excited by monochromatic plane waves whose wavelengths were (a) 3.33, (b) 1.89, and (c) 1.84 μm. The length of each vector was normalized and intensity was expressed using a color scale.

1.89 μm. Similar to the case for $w = 300$ nm, the strong electric field around the rectangular island exhibits polarized electric charges at the lower left and the right corners. However, the electric field around the island spreads along the interface between the vacuum and GaSb layers, and the capacitor, C_m, is not observed at the GaSb layer. The electric field distribution resembles the anti-reflection mode of the gold–GaSb bilayer shown in figure 8(c). In the case of the bilayer, the electric field is kept at zero along the interface between the gold and GaSb layers, while the electric field reaches maximum intensity at the GaSb–vacuum interface. A comparison between figures 8(b) and (c) implies that the electric charge in the polarized island layer cancels the electric field inside the island against external electric fields. Because neither the circuit nor the SRSP was formed between the top and bottom gold layers when the island width was comparatively smaller, the lumped-element and Fabry–Pérot interference models lost accuracy.

When the resonant wavelength of the lumped-element model is shorter than that of the anti-reflection mode, the capacitor, C_m, is not observed, as shown in figure 8(b). Therefore, circuit resonance is independently observed only when the lumped-element model shows a much longer wavelength than the anti-reflection mode. With increasing $\Lambda - w$, the first resonant angular frequency of the lumped-element model in equation (8) approximately approaches $\omega_r = 1/\sqrt{C_m(L_m + L_k)}$, and it is equivalent to the resonant wavelength, $\lambda_r = 2\pi c_0\sqrt{C_m(L_m + L_k)}$. The resonant wavelength, λ_r, has the following correlation:

$$\lambda_r \propto w\varepsilon'^{0.5}_{GaSb}, \tag{18}$$

and λ_r also has an inverse correlation to d, while it cannot be simply written. The wavelength of the anti-reflection mode is approximately $4n_{GaSb}d$. Thus, the island width and the semiconductor thickness need to be respectively large and small to observe circuit resonance. Empirically, the critical length of w is twice or three times the semiconductor thickness.

The discussions focusing on the identical electric charge inside the island showed deep relationships between the lumped-element and Fabry–Pérot interference models for the MSM multilayer with a sufficiently large island. The electric response at the circuit resonance frequency resembles the Fabry–Pérot interference for the SRSP mode, and the magnetic response at the Fabry–Pérot interference frequency is similar to the MP. As a result, the two physical models for the MSM multilayer indicate the same resonant mode at the near-infrared wavelength. Moreover, since the magnetic permeabilities of gold and GaSb are 1.0, the origin of the magnetic resonance called MP is a magnetic field excited by the SPP.

5. Conclusions

An MSM multilayer with an island geometry for the top metal layer and a thin GaSb as a middle layer were analyzed to clarify the distinguishability between the circuit resonance and Fabry–Pérot interference mediated by the SPP. The electromagnetic fields around the MSM multilayer were numerically determined using an FDTD method to obtain the spectral absorptance and electromagnetic field distribution. For the second resonant mode, the peak wavelength agreed to the lumped-element model, and the electromagnetic field distribution showed three pairs of electric charges corresponding to three capacitors used in the lumped-element model. Simultaneously, the electric charges formed longitudinal waves supporting the SRSP inside the GaSb layer. The SRSP interfered with itself at the GaSb region sandwiched between the two gold layers. As a result, the resonant wavelength also agreed with the Fabry–Pérot interference model considering the wavelength and phase retardation of the SPP. For the first mode, because the SPP expanded to the sidewall of the island, the effective capacitance of the circuit and phase retardation of the SPP increased slightly. Therefore, several modifications are required for both lumped-element and Fabry–Pérot interference models to improve the accuracy. The electric and magnetic fields respectively depicted the current loop and enhanced magnetic field described in earlier studies. However, the time-lapse visualization showed little contribution to the current loop for exciting the magnetic field. It also showed that both the lumped-element and Fabry–Pérot interference models indicated the same resonant mode, and the magnetic response at the GaSb layer originates a development of the SPP rather than the magnetic resonance or MP. Here, both the lumped-element and Fabry–Pérot interference models became invalid due to the anti-reflection mode of the gold–GaSb bilayer when the semiconductor thickness was greater than one-third of the island width. It is because the MSM multilayer with a small island could mediate neither the circuit nor the SRSP between the top and bottom gold layers.

Acknowledgments

The authors would like to thank the Japan Society for the Promotion of Science (JSPS) KAKENHI Grant in Aide (Number: 20H02084) for the financial support.

Data availability statement

The data that support the findings of this study are available upon reasonable request from the authors.

ORCID iDs

Kazuma Isobe https://orcid.org/0000-0002-8621-5015

References

[1] Luo C, Johnson S G, Joannopoulos J D and Pendry J 2003 Negative refraction without negative index in metallic photonic crystals *Opt. Express* **11** 746

[2] Smolyaninov I I, Smolyaninova V N, Kildishev A V and Shalaev V M 2009 Anisotropic metamaterials emulated by tapered waveguides: application to optical cloaking *Phys. Rev. Lett.* **102** 213901

[3] Matsumoto T, Koizumi T, Kawakami Y, Okamoto K and Tomita M 2013 Perfect blackbody radiation from a graphene nanostructure with application to high-temperature spectral emissivity measurements *Opt. Express* **21** 30964

[4] Lee B J, Wang L and Zhang Z M 2008 Coherent thermal emission by excitation of magnetic polaritons between periodic strips and a metallic film *Opt. Express* **16** 11328
[5] Wang L and Zhang Z M 2009 Resonance transmission or absorption in deep gratings explained by magnetic polaritons *Appl. Phys. Lett.* **95** 111904
[6] Liu X, Tyler T, Starr T, Starr A F, Jokerst N M and Padilla W J 2011 Taming the Blackbody with Infrared Metamaterials as Selective Thermal Emitters *Phys. Rev. Lett.* **107** 045901
[7] Tian Y, Ghanekar A, Ricci M, Hyde M, Gregory O and Zheng Y 2018 A review of tunable wavelength selectivity of metamaterials in near-field and far-field radiative thermal transport *Materials* **11** 1–19
[8] Long L, Taylor S, Ying X and Wang L 2019 Thermally-switchable spectrally-selective infrared metamaterial absorber/emitter by tuning magnetic polariton with a phase-change VO_2 layer *Materials Today Energy* **13** 214–20
[9] Wang J, Yang L, Wang M, Hu Z-D, Deng Q, Nie Y, Zhang F and Sang T 2019 Perfect absorption and strong magnetic polaritons coupling of graphene-based silicon carbide grating cavity structures *J. Phys. D: Appl. Phys.* **52** 015101
[10] Zhou J, Koschny T, Kafesaki M, Economou E N, Pendry J B and Soukoulis C M 2005 Saturation of the magnetic response of split-ring resonators at optical frequencies *Phys. Rev. Lett.* **95** 223902
[11] Dolan J A *et al* 2016 Gyroid optical metamaterials: Calculating the effective permittivity of multidomain samples *ACS Photonics* **3** 1888–96
[12] Sakurai A, Yada K, Simomura T, Ju S, Kashiwagi M, Okada H, Nagao T, Tsuda K and Shiomi J 2019 Ultranarrow-band wavelength-selective thermal emission with aperiodic multilayered metamaterials designed by bayesian optimization *ACS Central Science* **5** 319–26
[13] Engheta N 2007 Circuits with light at nanoscales: Optical nanocircuits inspired by metamaterials *Science (1979)* **317** 1698–702
[14] Zhang Y, Qiao S, Sun L, Shi Q W, Huang W, Li L and Yang Z 2014 Photoinduced active terahertz metamaterials with nanostructured vanadium dioxide film deposited by sol-gel method *Opt. Express* **22** 11070
[15] Bao Z, Wang J, Hu Z-D, Chen Y, Zhang C and Zhang F 2021 Coordination multi-band absorbers with patterned irrelevant graphene patches based on multi-layer film structures *J. Phys. D: Appl. Phys.* **54** 505306
[16] O'Brien S and Pendry J B 2002 Magnetic activity at infrared frequencies in structured metallic photonic crystals *J. Phys. Condens. Matter* **14** 6383–94
[17] Grigorenko A N, Geim A K, Gleeson H F, Zhang Y, Firsov A A, Khrushchev I Y and Petrovic J 2005 Nanofabricated media with negative permeability at visible frequencies *Nature* **438** 335–8
[18] Sarychev A K, Shvets G and Shalaev V M 2006 Magnetic plasmon resonance *Phys. Rev. E* **73** 036609
[19] Li T, Li J Q, Wang F M, Wang Q J, Liu H, Zhu S N and Zhu Y Y 2007 Exploring magnetic plasmon polaritons in optical transmission through hole arrays perforated in trilayer structures *Appl. Phys. Lett.* **90** 1–4
[20] Li T, Wang S M, Liu H, Li J Q, Wang F M, Zhu S N and Zhang X 2008 Dispersion of magnetic plasmon polaritons in perforated trilayer metamaterials *J. Appl. Phys.* **103** 023104
[21] Sakurai A, Zhao B and Zhang Z M 2014 Resonant frequency and bandwidth of metamaterial emitters and absorbers predicted by an RLC circuit model *J. Quant. Spectrosc. Radiat. Transfer* **149** 33–40
[22] Guo Y, Xiong B, Shuai Y and Zhao J 2020 Thermal driven wavelength-selective optical switch based on magnetic polaritons coupling *J. Quant. Spectrosc. Radiat. Transfer* **255** 107230
[23] Wang L and Zhang Z M 2011 Phonon-mediated magnetic polaritons in the infrared region *Opt. Express* **19** A126
[24] Zhang B, Li Z, Hu Z, Zhang J and Wang J 2022 Analysis of a bidirectional metamaterial perfect absorber with band-switchability for multifunctional optical applications *Results in Physics* **34** 105313
[25] Huang H, Xia H, Xie W, Guo Z, Li H and Xie D 2018 Design of broadband graphene-metamaterial absorbers for permittivity sensing at mid-infrared regions *Sci. Rep.* **8** 4183
[26] Isobe K, Okino R and Hanamura K 2020 Spectral absorptance of a metal–semiconductor–metal thin-multilayer structured thermophotovoltaic cell *Opt. Express* **28** 40099–111
[27] Ni Q, Alshehri H, Yang Y, Ye H and Wang L 2018 Plasmonic light trapping for enhanced light absorption in film-coupled ultrathin metamaterial thermophotovoltaic cells *Frontiers in Energy* **12** 185–94
[28] Feng R, Qiu J, Liu L, Ding W and Chen L 2014 Parallel LC circuit model for multi-band absorption and preliminary design of radiative cooling *Opt. Express* **22** A1713
[29] Ma W, Wen Y and Yu X 2013 Broadband metamaterial absorber at mid-infrared using multiplexed cross resonators *Opt. Express* **21** 30724
[30] Dicken M J, Aydin K, Pryce I M, Sweatlock L A, Boyd E M, Walavalkar S, Ma J and Atwater H A 2009 Frequency tunable near-infrared metamaterials based on VO_2 phase transition *Opt. Express* **17** 18330
[31] Hyde P, Bai L, Harder M, Dyck C and Hu C-M 2017 Linking magnon-cavity strong coupling to magnon-polaritons through effective permeability *Physical Review B* **95** 094416
[32] Nambu Y *et al* 2020 Observation of magnon polarization *Phys. Rev. Lett.* **125** 027201
[33] Liu T and Takahara J 2017 Ultrabroadband absorber based on single-sized embedded metal-dielectric-metal structures and application of radiative cooling *Opt. Express* **25** A612
[34] Howell J R, Siegel R and Mengüç M P 2011 *Thermal Radiation Heat Transfer* (New York: CRC Press)
[35] Oskooi A F, Roundy D, Ibanescu M, Bermel P, Joannopoulos J D and Johnson S G 2010 Meep: A flexible free-software package for electromagnetic simulations by the FDTD method *Comput. Phys. Commun.* **181** 687–702
[36] Palik E D 1985 *Handbook of Optical Constants of Solids* 1 (San Diego, California: Academic)
[37] Adachi S 1989 Optical dispersion relations for GaP, GaAs, GaSb, InP, InAs, InSb, $Al_xGa_{1-x}As$, and $In_{1-x}Ga_xAs_yP_{1-y}$ *J. Appl. Phys.* **66** 6030–40
[38] Kelley D F and Luebbers R I 1996 Piecewise linear recursive convolution for dispersive media using FDTD *IEEE Trans. Antennas Propag.* **44** 792–7
[39] Berenger J-P 1994 A perfectly matched layer for the absorption of electromagnetic waves *J. Comput. Phys.* **114** 185–200
[40] Correia D and Jian-Ming J 2005 *2006 On the development of a higher-order PML SBMO/IEEE MTT-S Int. Conf. on Microwave and Optoelectronics* 53 *(Piscataway, NJ)* (IEEE) 578–80
[41] Chen Y B and Chiu F C 2013 Trapping mid-infrared rays in a lossy film with the Berreman mode, epsilon near zero mode, and magnetic polaritons *Opt. Express* **21** 20771
[42] Ashcroft N W and Mermin N D 1976 *Solid State Physics* (Philadelphia: College: Saunders Publishing)
[43] Zhou J, Economou E N, Koschny T and Soukoulis C M 2006 Unifying approach to left-handed material design *Opt. Lett.* **31** 3620
[44] Francoeur M, Mengüç M P and Vaillon R 2009 Solution of near-field thermal radiation in one-dimensional layered media using dyadic Green's functions and the scattering matrix method *J. Quant. Spectrosc. Radiat. Transfer* **110** 2002–18

[45] Economou E N 1969 Surface plasmons in thin films *Phys. Rev.* **182** 539–54
[46] Bai W, Gan Q, Song G, Chen L, Kafafi Z and Bartoli F 2010 Broadband short-range surface plasmon structures for absorption enhancement in organic photovoltaics *Opt. Express* **18** A620